Reverse convection potential saturation during northward IMF under various driving conditions

F. D. Wilder,[1] C. R. Clauer,[1] and J. B. H. Baker[1]

Received 17 March 2009; revised 29 April 2009; accepted 4 June 2009; published 14 August 2009.

[1] We report the results of an investigation of the reverse convection potentials in the dayside high-latitude ionosphere during periods of steady northward interplanetary magnetic field (IMF). While it has been demonstrated that the reverse convection potentials exhibit saturation behavior, an investigation into how the saturated reverse convection cells respond to various driving conditions has not yet been performed. We use the OMNI database from 1998 to 2007 to search for events in solar wind data propagated to the bow shock when the IMF is northward and when various driving parameters are stable for more than 40 min. We then use bin-averaged SuperDARN Doppler radar velocity data to apply a spherical harmonic fit to calculate the average potential pattern for various driving conditions. Results show that the saturated reverse convection potential during northward IMF is substantially lower than during southward IMF (as expected), but the strength of the saturation electric field at a particular location is comparable during northward IMF to what it is during southward IMF. Seasonal dependence and dependence on the Alfvènic Mach number and solar wind β are also investigated. It appears that the reverse convection potential demonstrates the opposite of what is expected for seasonal dependence, and that the Alfvènic Mach number is not the fundamental driver of its saturation.

Citation: Wilder, F. D., C. R. Clauer, and J. B. H. Baker (2009), Reverse convection potential saturation during northward IMF under various driving conditions, *J. Geophys. Res.*, *114*, A08209, doi:10.1029/2009JA014266.

1. Introduction

[2] The primary mechanism whereby energy and momentum are coupled to the magnetosphere from the solar wind is the process of magnetic reconnection on the dayside of the Earth [*Dungey*, 1961]. When two regions of plasma containing antiparallel magnetic fields collide at high-enough dynamic pressure, it will cause the magnetic fields to merge and shear in an X-shaped formation. These newly sheared magnetic field lines will experience high Maxwell stress and be pulled to the nightside of Earth, where they will reconnect and split in the tail. This reconnection in turn drives convection in the polar ionosphere.

[3] Another mechanism described as a viscous-like interaction is also thought to couple energy to the magnetosphere from the solar wind, but at a rate which is small compared to reconnection [*Axford and Hines*, 1961]. During geomagnetically quiet periods when the driving of the magnetosphere by reconnection is negligible, there continues to be a background convection pattern driven by this viscous interaction. The electric potential across the magnetosphere during quiet periods has been estimated to be 20 kilovolts [*Papitashvili et al.*, 1981].

[4] The magnetospheric convection that results from a combination of magnetic reconnection and viscous interactions maps along magnetic field lines into the high-latitude ionosphere to generate plasma convection and an associated polar electric potential [*Dungey*, 1961; *Axford and Hines*, 1961]. When the IMF points southward and reconnection occurs at the subsolar point, the result is a two-cell convection pattern with antisunward flow at the highest latitudes. The cross polar cap potential, Φ_{PC}, associated with this pattern is an important metric of the energy flow through the coupled magnetosphere-ionosphere system. During instances of strongly southward IMF, the polar cap potential as a function of solar wind electric field has been observed to experience nonlinear "saturation" [*Siscoe et al.*, 2002b; *Shepherd et al.*, 2002; *Hairston et al.*, 2005].

[5] When the IMF is northward, reconnection occurs poleward of the cusp on lobe field lines in the Earth's magnetosphere [*Dungey*, 1963; *Watanabe et al.*, 2005; *Dorelli et al.*, 2007]. The resulting convection pattern consists of four cells. Two cells contain antisunward flow at higher latitudes and sunward return flow at low latitudes caused by viscous interactions. The other two are reverse convection cells at high latitude on the dayside that exist as a result of lobe reconnection [*Crooker*, 1992]. The reverse convection cells are thought to be driven by high-latitude field aligned currents termed NBZ [*Iijima et al.*, 1984]. NBZ refers to the fact that the field aligned currents form when the IMF B_Z is directed northward.

[1]Bradley Department of Electrical and Computer Engineering, Virginia Tech, Blacksburg, Virginia, USA.

0148-0227/09/2009JA014266

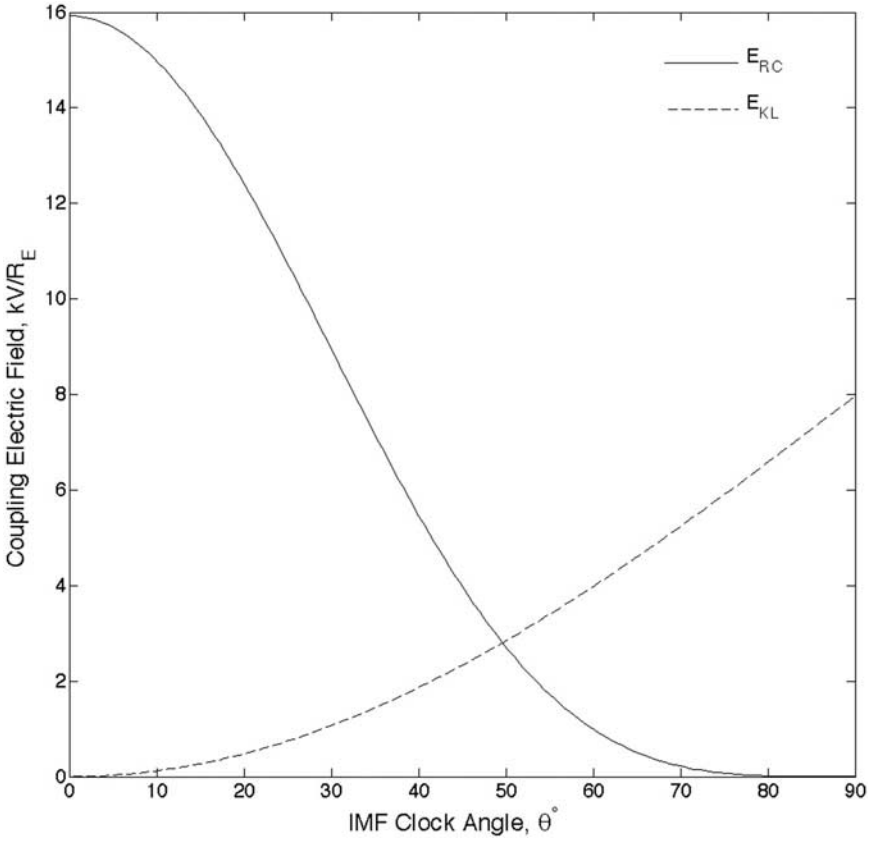

Figure 1. Comparison between E_{RC} and E_{KL}, represented by the solid and dashed line, respectively. For both cases, the IMF magnitude was set to 5 nT and the antisunward velocity was 500 km/s as the IMF clock angle was varied.

[6] *Wilder et al.* [2008] used Super Dual Auroral Radar Network (SuperDARN) Doppler velocity measurements to demonstrate that the electric potential across the vortices driven by the NBZ Currents, Φ_{RC}, also exhibits nonlinear saturation behavior. The method used was to create bins of events where the solar wind electric field stayed stable within a minimum and maximum value for a minimum of 40 min. For each solar wind electric field bin, SuperDARN Doppler velocity vectors from each event were then filtered in a manner which generated the most likely convection pattern. A spherical harmonic fit was then applied to determine the electric potential pattern for each solar wind electric field bin. The potential across the reverse convection cells saturated at approximately 20 kV [*Wilder et al.*, 2008].

[7] While *Wilder et al.* [2008] demonstrated that the NBZ cells exhibit saturation behavior, the cause of this saturation was not investigated. For southward IMF, studies have shown the effect of various driving parameters such as dynamic pressure and Alfvènic Mach number on the saturation of the polar cap potential [*Siscoe et al.*, 2002a; *Ridley*, 2007]. There have not yet been any studies to our knowledge on the response of the four cell pattern formed under northward IMF to various driving conditions. Also, there is a difference in conductivity between the winter and summer hemispheres because of the lack of photoionization in the winter, so separating out events of strong northward IMF by season will shed light on the response of the four cell pattern to variations in ionospheric conductivity [*Fujii et al.*, 1981].

[8] The purpose of this study is to build upon the *Wilder et al.*'s [2008] results and investigate the effects of various solar wind driving conditions as well as ionospheric conductivity on the saturation potential and electric field of the NBZ cells. A clearer picture of the relationship between the saturation of Φ_{PC} and Φ_{RC} will also be demonstrated. We expand on the results presented by *Wilder et al.* [2008], showing the saturation of the reverse convection electric field under northward IMF, as well as the dependence of Φ_{RC} on Alfvènic Mach number and solar wind β. It will be demonstrated that there is a clear seasonal dependence of the reverse convection potential pattern, and that the reverse convection potential still saturates even when the Alfvènic Mach number is nominal. Also, there is a clear dependence of the reverse convection potential under strong northward IMF driving on solar wind plasma β.

2. Methodology

2.1. Solar Wind Selection Criteria

[9] *Sonnerup* [1974] proposed a geometric coupling function which could serve as a metric for the electric field coupled into the magnetosphere during subsolar magnetic reconnection, E_{KL}, given by

$$E_{KL} = VB_T \sin^2 \frac{\theta}{2} \tag{1}$$

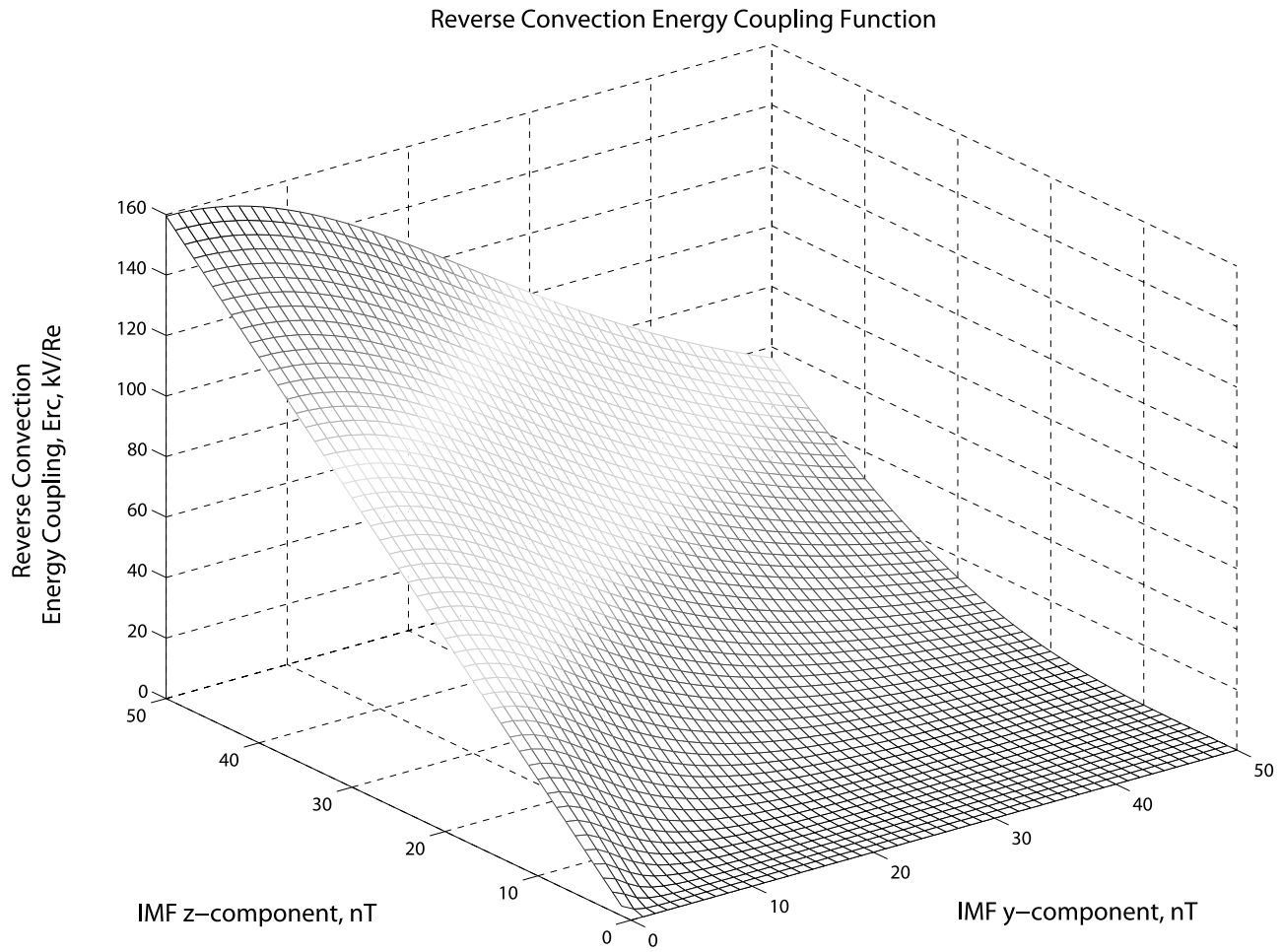

Figure 2. Reverse convection energy coupling function E_{RC} as a function of B_Z and B_Y.

[10] Where V is the antisunward component of the solar wind velocity, $B_T = \sqrt{B_Z^2 + B_Y^2}$ is the component of the IMF transverse to V, and $\theta = \cos^{-1}\frac{B_Z}{B_T}$ is the IMF clock angle in the (Y-Z) plane [*Kan and Lee*, 1979; *Sonnerup*, 1974]. Several studies have used this parameter to correlate the solar wind with the polar cap potential [*Reiff et al.*, 1981; *Weimer*, 1995; *Shepherd et al.*, 2002]. While E_{KL} is useful in measuring the polar ionospheric response to southward IMF conditions, it can be seen from the sinusoidal term that at periods of purely northward IMF, E_{KL} will be zero. Thus in order to provide a measure of the electric field coupling from lobe reconnection into the magnetosphere under northward IMF, the reverse convection coupling function from *Wilder et al.* [2008], E_{RC}, was used. E_{RC} is similar to E_{KL}, except with geometric factors modified to select events with strongly northward IMF. The final form of E_{RC} is given by

$$E_{RC} = VB_T \cos^n \theta \tag{2}$$

[11] Where n is an integer. A value of $n = 4$ was chosen to ensure that large values of E_{RC} corresponded to high IMF B_Z more than B_Y. Figure 1 shows a comparison between E_{RC} and E_{KL} versus IMF clock angle. It is evident that at $\theta = 0°$, which corresponds to a purely northward IMF, E_{KL} is zero and E_{RC} is at a maximum. This demonstrates that E_{KL} cannot be used as a coupling function for northward IMF. It should be noted that when selecting events in solar wind data, events with a clock angle greater than 90° were immediately discarded. Figure 2 shows the value of E_{RC} as the IMF B_Y and B_Z vary and demonstrates that E_{RC} is designed to select events with small values of B_Y in comparison to B_Z. *Wilder et al.* [2008] demonstrated that the form of E_{RC} given here minimizes the effect of the IMF B_Y on each bin chosen.

[12] Using E_{RC} and various driving parameters for solar wind-magnetosphere-ionosphere coupling, events can be found that fit very specific criteria. In order to increase the resolution of the *Wilder et al.* [2008] result, events were found using propagated 1-min data from the OMNI database between 1998 to 2007 [*King and Papitashvili*, 2005]. This new data set adds 2 more years of solar wind data to the study, as *Wilder et al.* [2008] only used data from 1998 to 2005. Events of quasi-stable E_{RC} were placed into bins containing a minimum and maximum E_{RC} value. The stability criteria on E_{RC} was that an event would stay within the minimum and maximum value for at least 40 min. The range for each bin was selected to maximize the spatial coverage of Doppler measurements within each bin, but at the same time provide enough discretization in a plot of the

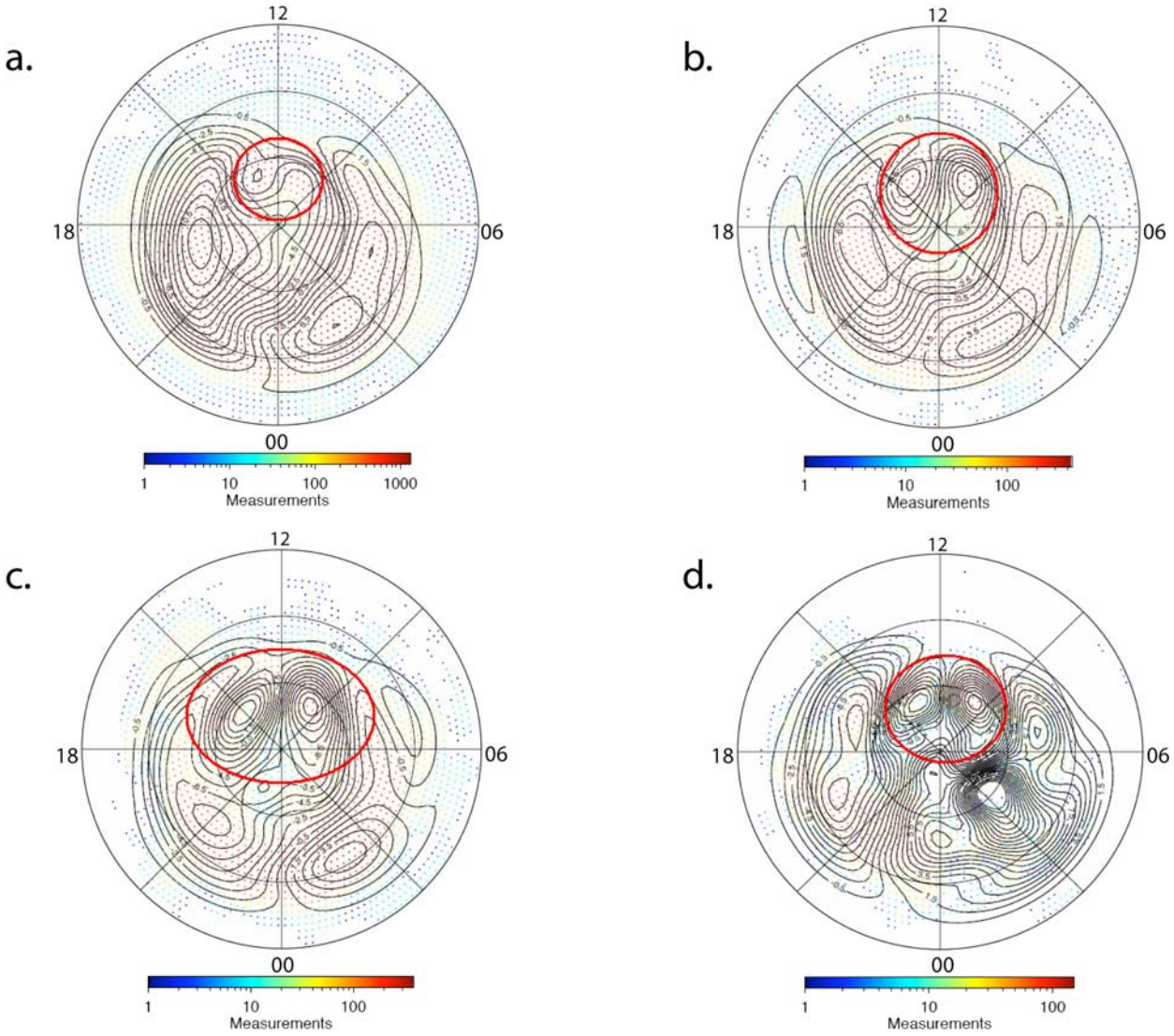

Figure 3. Calculated four cell convection pattern for four E_{RC} bins: (a) 2 to 4 kV/Re, (b) 10 to 13 kV/Re, (c) 19 to 23 kV/Re, and (d) 32 to 39 kV/Re. The dayside convection cells are circled in red. Corresponding reverse convection potentials are (a) 2.85 kV, (b) 10.66 kV, (c) 17.44 kV, and (d) 19.36 kV.

potential versus electric field driving to show a possible saturation effect.

[13] A method of overlapping bins was also used at higher values of E_{RC}. Because the range of E_{RC} in each solar wind driving bin must widen as E_{RC} gets larger in order to ensure sufficient spatial coverage in the ionosphere, overlapping bins help to show the overall trend for Φ_{RC} while demonstrating whether or not events around the minimum and maximum E_{RC} for each bin are having an effect on the measurement of Φ_{RC}. This method was also used by *Wilder et al.* [2008].

[14] 925 events were used to generate the plot of Φ_{RC} versus E_{RC}, compared to 892 used in [*Wilder et al.*, 2008]. This allowed for more bins with stronger driving, giving a better idea of the behavior of Φ_{RC}. Using data from 2006 and 2007 was also beneficial for the overall study because it allowed for the use of the higher-latitude PolarDARN radars [*Chisham et al.*, 2007].

2.2. Generation of Reverse Convection Potential Patterns

[15] Global convection patterns from which Φ_{RC} was found were then calculated using the Super Dual Auroral Radar Network (SuperDARN) [*Chisham et al.*, 2007]. SuperDARN is a network of high-latitude coherent scatter radars that make Doppler measurements of line-of-sight ionospheric plasma convection velocities. Overlapping coverage between radars allows for two dimensional convection patterns to be deduced. Coefficients of a spherical harmonic expansion are then fit to the velocity vectors to determine the electric potential pattern in the polar ionosphere [*Ruohoniemi and Baker*, 1998].

[16] It is difficult to measure the reverse convection potential for individual events using SuperDARN radar data. Oftentimes, coverage of the reverse convection cells can be spotty in an individual event, resulting in a fitted

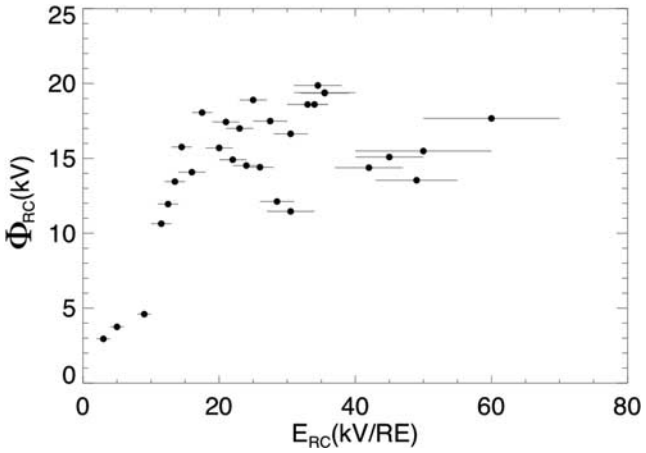

Figure 4. Reverse convection potential, Φ_{RC}, as a function of E_{RC}. The marks represent the center of the bins, and the horizontal lines represent the width of each bin in kV/Re.

potential pattern based primarily on statistical model vectors. Because of this, averaging the potential patterns of all events in an E_{RC} bin will result in either weak or nonexistent reverse convection patterns, which could even misleadingly force a saturation result. The method in this study relies on the principle of superposition, as well as preprocessing the line of sight velocity vectors (VLOS) in order to generate the most likely convection pattern for an E_{RC} bin. This method requires no model vectors to fill in the pattern, and could be viewed as a spatial analogue to the superposed epoch technique. The steps taken to generate the reverse convection potential are as follows.

[17] 1. The map of the polar cap is divided into 100 km by 100 km spatial bins. These spatial bins are then divided further into bins of VLOS directions in ten degree increments of magnetic azimuth from −90 to 90 degrees.

[18] 2. VLOS vectors from the SuperDARN for all events within the E_{RC} bin were then placed in their respective spatial bin. This allows patterns with coverage in different parts of the reverse convection potential cells to be superposed.

[19] 3. For each spatial bin, it is determined whether the majority of measurements are positive or negative. The median positive or negative value is then chosen based on which dominates. This reduces data going into the spherical harmonic fitter, and smoothes out large positive and negative values which cancel in the fitter at convection reversal boundaries [*Ruohoniemi and Baker*, 1998].

[20] 4. A spherical harmonic fitting technique is then applied to the resulting gridded velocity measurements. Here, the electric field in the ionosphere is assumed to be the gradient of the electric potential, with equipotential lines that are the streamlines of the plasma convection. A potential pattern is then determined using a least squares fit of coefficients of a spherical harmonic expansion to the convection data [*Ruohoniemi and Baker*, 1998].

[21] 5. Once an E_{RC} bin's potential pattern is determined, the reverse convection potential is measured by taking the difference between the minimum and maximum potential of the high-latitude reverse cells. This is done manually to ensure that the potential across the reverse cells is measured instead of the potential between a reverse cell and a lobe cell.

[22] Figure 3, for example, shows four convection patterns as the IMF turns increasingly northward. These are the same patterns used in [*Wilder et al.*, 2008], and are generated using the statistical fitting method described above. Each pattern is presented in AACGM MLAT-MLT format with the magnetic pole at the center and magnetic noon directed up the page. The lowest latitude shown is 60 degrees and the contour spacing is 1kV. Color-coding shows the number of gridded SuperDARN measurements that contributed to the calculation of each pattern. The four convection patterns in Figure 3 correspond to the following bins of E_{RC}: (1) 2–4, (2) 10–13, (3) 19–23, and (4) 32–39 kV/Re. The values of the reverse convection potential, Φ_{RC}, are 2.85, 10.66, 17.44, and 19.36 kV respectively. As E_{RC} increases, the reverse convection potential cells become more prominent and then saturate at the largest values of E_{RC} [*Wilder et al.*, 2008].

[23] Figure 4 demonstrates the nonlinear behavior of the reverse convection potential as E_{RC} increases, using the same bins as *Wilder et al.* [2008] in addition to several more bins at increasingly large values of E_{RC}. These bins include 40 to 60 kV/R_E and 50 to 70 kV/Re. A bin ranging from 50 to 150 kV/Re was also examined with a potential found to be 20.49 kV. For the bins of E_{RC}, saturation occurs when the reverse convection reaches approximately 20 kV and when E_{RC} reaches above 18 kV/Re. It should be noted that this is by no means a maximum potential, as these are statistical patterns.

[24] In order to validate the result, one can measure the potential across the lobe cells, also known as the viscous potential, in the four cell pattern and ensure that the method yields the expected result. Figure 5 shows the behavior of the viscous potential, Φ_{PC}, as E_{RC} increases. The viscous potential remains around 20 kV, with larger values that are not unreasonable for viscous interactions [*Papitashvili et al.*, 1981]. The bins where the viscous potential exceeded 25 kV contained a larger amount of events in the winter months when the ionospheric conductivity is lower, which

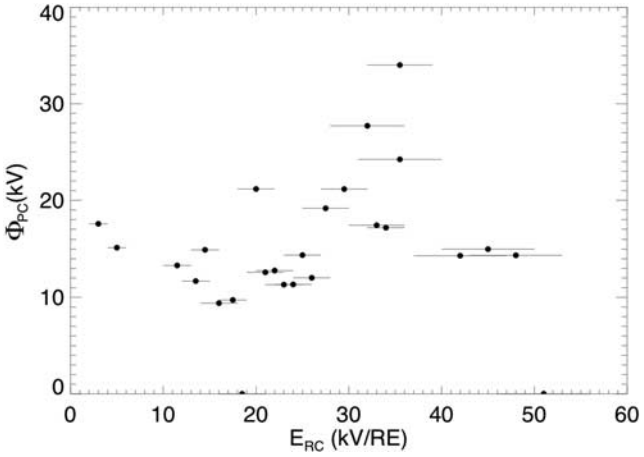

Figure 5. Potential across the viscous cells, Φ_{PC}, as a function of E_{RC}. The marks represent the center of the bins, and the horizontal lines represent the width of each bin in kV/Re.

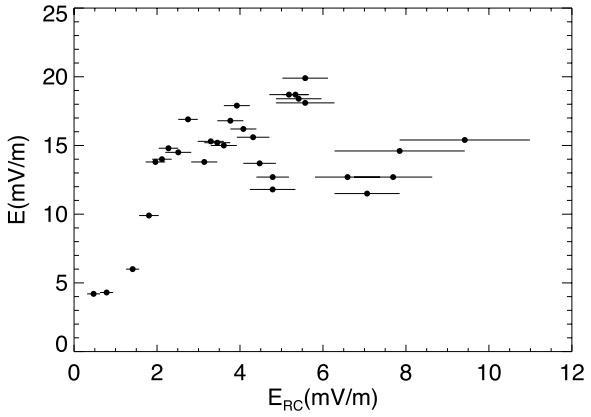

Figure 6. Electric field across the reverse convection cells as a function of E_{RC}. The marks represent the center of the bins, and the horizontal lines represent the width of each bin in mV/m.

leads to larger polar cap potentials. Values of exceedingly low viscous potential are found in bins where the viscous convection cells had significantly less coverage than the NBZ cells.

[25] Figure 4 shows that the saturation potential in this study for Φ_{RC} is around 20 kV. This is very small in comparison to the southward IMF saturation potential of Φ_{PC}, which has been shown to be approximately 100 kV using SuperDARN measurements [*Shepherd et al.*, 2002]. It should be noted, however, that during events of extreme driving under southward IMF, the size of the polar cap becomes significantly larger than the distance between the centers of the NBZ cells under northward IMF. This difference in polar cap size makes comparison between saturated Φ_{RC} and Φ_{PC} as well as the determination of the saturation Φ_{PC} more difficult. It should be noted, however, that the electric field across two potential cells is inversely proportional to the distance across them, as noted by an electrostatic approximation of Faraday's Law [*Jackson*, 1975]. Therefore while the maximum potential across the reverse convection cells is significantly smaller than the saturation potential for southward IMF, the difference between the distance across the reverse convection cells and the polar cap size under extreme southward IMF can lead to comparable electric fields.

[26] In order to calculate the electric field from Φ_{RC}, the great circle distance formula, given by equation (3), was used on the basis of magnetic latitude and magnetic longitude of the center of each NBZ cell.

$$d = Re\cos^{-1}\left[\sin\theta_1\sin\theta_2 + \cos\theta_1\cos\theta_2\cos\Delta\phi\right] \qquad (3)$$

[27] Where d is the great circle distance, Re is the Earth's radius, θ_1 and θ_2 are the longitudes of the center of each cell, and $\Delta\phi$ is the difference in latitude between the centers of the NBZ cells [*Pearson*, 1990]. In order to obtain the electric field across the cells, the potential is divided by the great circle distance, which on average tends to be approximately 1000 km. This distance is approximately a quarter of the polar cap diameter measured by imaging satellites during storm time southward IMF intervals [*Rastätter et al.*, 2005].

[28] Figure 6 shows the behavior of the electric field across the reverse convection cells. E_{RC} is expressed in mV/m in order to directly compare with the electric field of the NBZ cells (1 mV/m $\approx$ 6.4 kV/Re). The electric field of the reverse cells begins to saturate at approximately 20 mV/m. It is likely that individual events can have larger and smaller electric fields, as these are statistical patterns. It should be noted that since the distance across the reverse convection cells is approximately one-fourth the polar cap size under southward IMF, and that the Φ_{RC} saturates at approximately one-fourth the saturated Φ_{PC} measured by *Shepherd et al.* [2002], then the electric field across both the saturated reverse cells and the saturated southward IMF potential pattern should be comparable.

[29] It is worth noting at this point that there is a discrepancy between the saturation potentials measured by SuperDARN and DMSP under Southward IMF [*Shepherd et al.*, 2002; *Hairston et al.*, 2005]. In the past, this has been explained by the fact that the polar cap expands equatorward during increasingly strong driving, which could mean that the potential pattern is outside the SuperDARN radars' fields of view [*Hairston et al.*, 2005]. Recent studies, however, have compared line of site velocity vectors measured by SuperDARN with DMSP cross-track plasma drift measurements and shown that the velocities measured by SuperDARN are 0.3 to 0.7 times smaller than those measured by DMSP [*Drayton et al.*, 2005; *Xu et al.*, 2007]. *Sundberg et al.* [2009] showed saturation of Φ_{RC} using DMSP and also demonstrated it to occur at approximately one fourth the saturation Φ_{PC} under southward IMF observed by *Hairston et al.* [2005].

3. Seasonal Dependence

[30] To help determine the effect of ionospheric conductivity on the four cell convection pattern which is formed under northward IMF, a comparison of statistical patterns from both the summer and winter ionosphere can be used. It is expected that during winter months, the ionospheric conductivity is lower because of reduced ionization from solar photons, thus increasing the electric potential by Ohm's law. One can determine how the saturation of the reverse convection cells varies on the basis of conductivity by examining Φ_{RC} under strong driving.

[31] In order to generate these patterns, two bins of E_{RC} from 18 to 60 kV/Re were used: one where all events were within 30 days of the winter solstice, and one where all events were within 30 days of the summer solstice. Statistical patterns were then generated using the APLFIT technique described in section 2. Figure 7 shows the E_{RC} behavior for the events used to generate a statistical pattern for the summer ionosphere, and Figure 8 demonstrates the E_{RC} behavior for the winter ionosphere. Comparison between Figures 7 and 8 shows that there is little significant difference in the distribution of solar wind electric field driving for either pattern.

[32] Figure 9 shows four cell convection patterns for both the winter and summer seasons. It can be seen that the resulting reverse convection potentials show the opposite of what would be expected. Φ_{RC} is 11.45 kV in the winter and

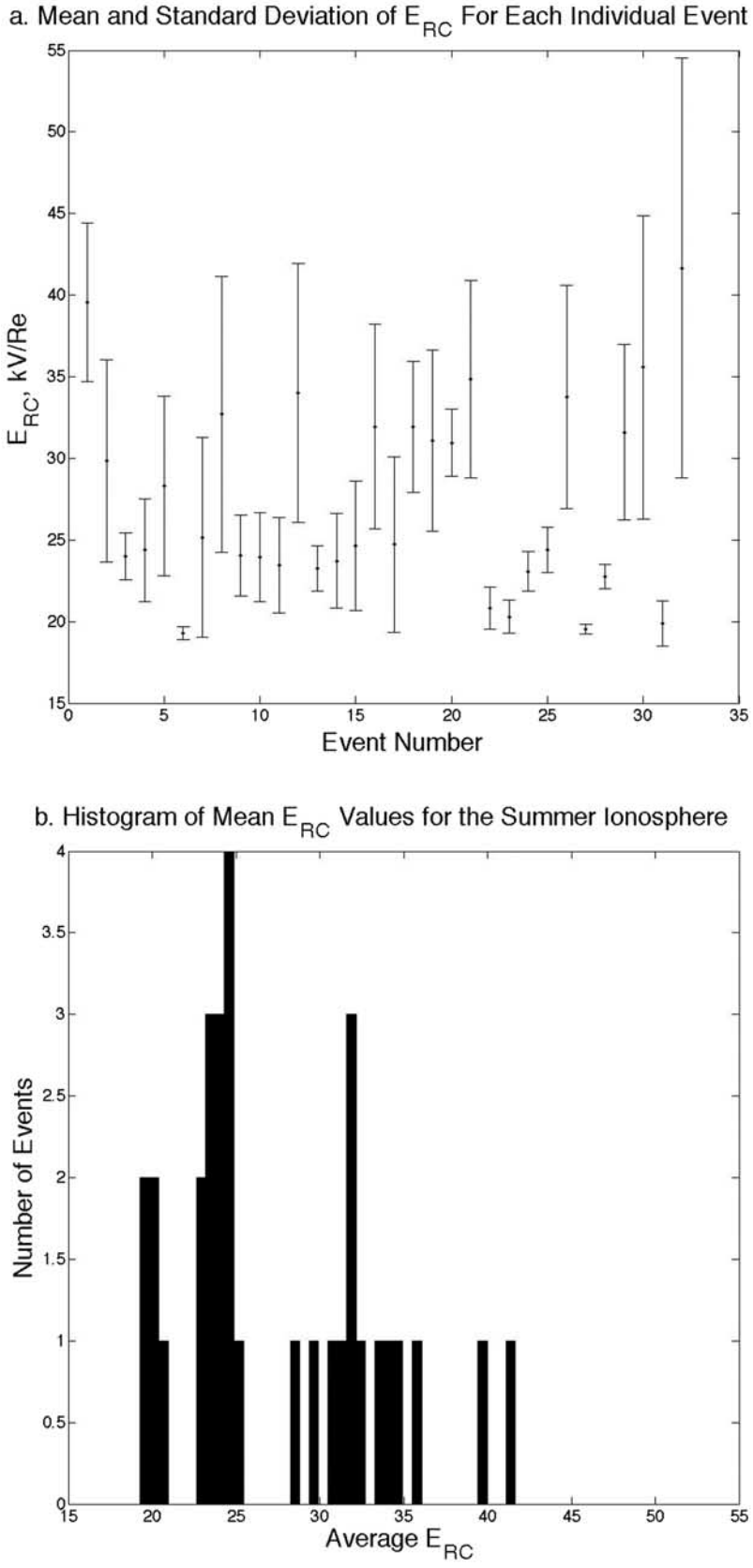

Figure 7. Statistics for the events within 30 days of the summer solstice. (a) Each point on the *x* axis is an individual event within the summer bin, with the marks indicating the mean value of E_{RC} and the error bars along the *y* axis the standard deviation of E_{RC}. (b) Histogram demonstrating the distribution of mean E_{RC} values over the entire summer bin.

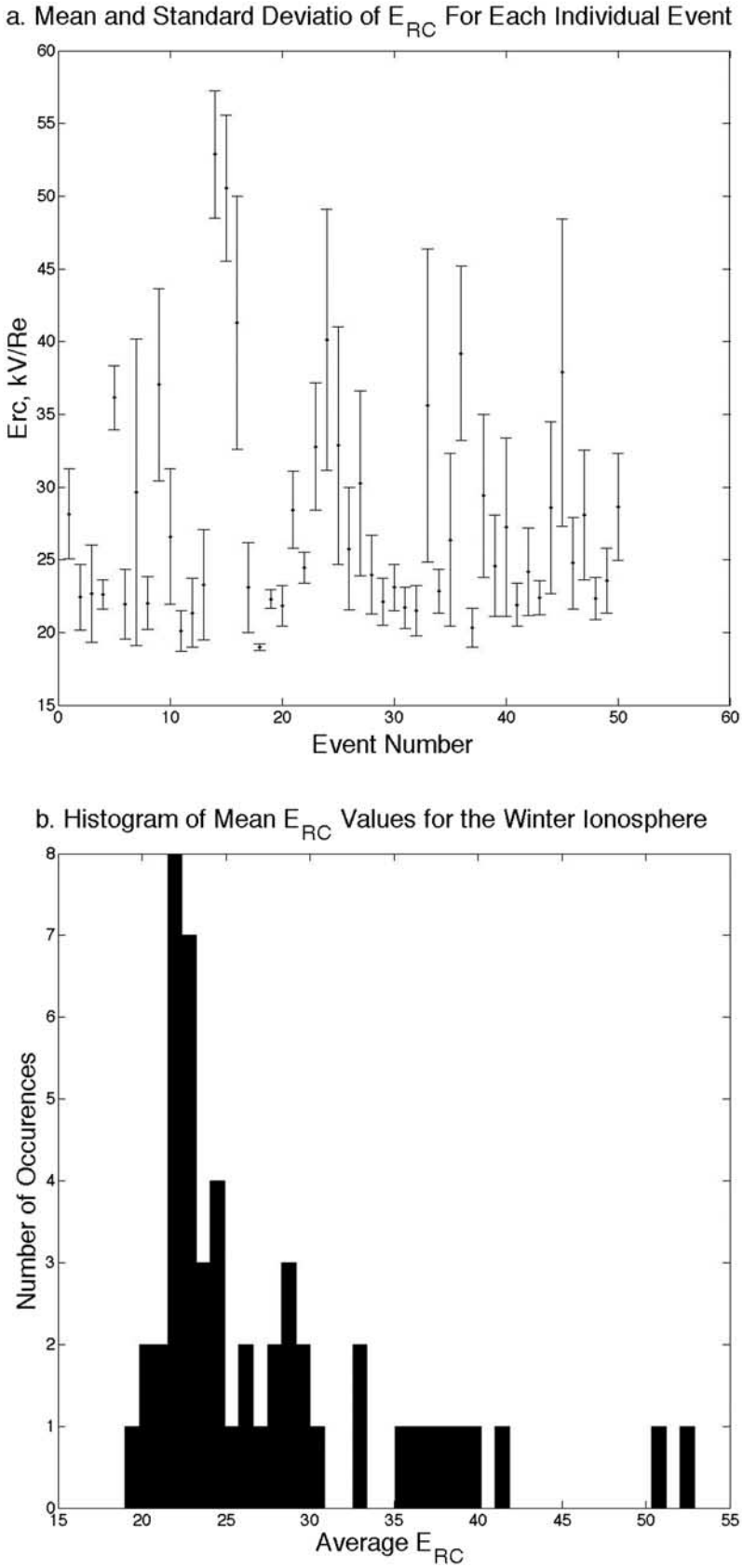

Figure 8. Statistics for the events within 30 days of the winter solstice. (a) Each point on the *x* axis is an individual event within the winter bin, with the marks indicating the mean value of E_{RC} and the error bars along the *y* axis the standard deviation of E_{RC}. (b) A histogram demonstrating the distribution of mean E_{RC} values over the entire winter bin.

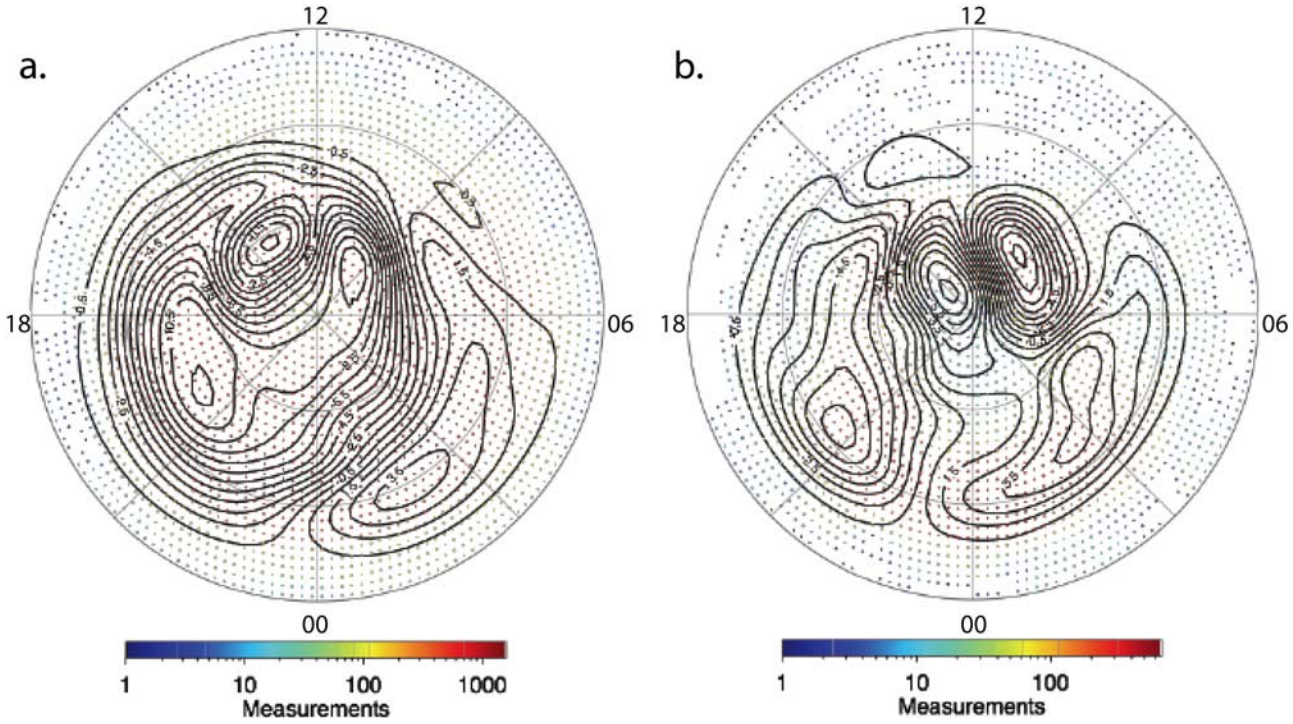

Figure 9. Calculated four cell convection patterns for both the (a) winter and (b) summer ionospheres within the saturation regime (E_{RC} greater than 18 kV/Re). The corresponding reverse convection potentials are (a) 11.45 kV and (b) 16.75 kV, with electric fields of (a) 11.5 mV/m and (b) 19 mV/m.

16.5 kV in the summer, with electric fields of 11.5 mV/m and 19 mV/m respectively. With a winter ionosphere at a lower conductivity than summer, one would expect Φ_{RC} to be larger from Ohm's law. The opposite occurs for the NBZ cells. It should be noted, however, that the viscous cells do exhibit the expected behavior, with far more prominent potential cells and stronger antisunward flow in the winter ionosphere. It seems as the antisunward convection caused by viscous interactions becomes increasingly strong, the sunward convection in the NBZ cells seems to be weaker, leading to less prominent reverse convection potential cells. This indicates that the NBZ field aligned currents caused by lobe reconnection not only close with themselves in the ionosphere, but also with the region 1 current system.

4. Alfvènic Mach Number Dependence

[33] Since *Ridley* [2007] suggested that Alfvèn wings can lead to saturation of polar cap potentials under both northward and southward IMF, it is useful to test the effect of Alfvènic Mach number on the reverse convection potential under northward IMF. The speed at which an Alfvèn wave travels in a plasma is the "Alfvèn Speed" and is given by

$$V_A = B/\sqrt{\mu_0 \rho} \tag{4}$$

where V_A is the Alfvèn speed, B is the magnitude of the magnetic field, μ_0 is the permeability of free space and ρ is the mass density of the plasma [*Kivelson and Ridley*, 2008]. The Alfvènic Mach number, M_A, is the ratio between the bulk flow of the plasma and its Alfvèn speed. Galilean satellites such as Io and Ganymede are embedded in sub-Alfvènic plasma corotating with Jupiter within its magnetosphere. As a result, when the plasma containing a frozen-in magnetic field encounters these obstacles and the magnetic field bends, Alfvèn waves are launched along the magnetic field lines, resulting in two tubes above and below the satellite where the flow characteristics of the plasma are altered. These tubes are called "Alfvèn wings" [*Neubauer*, 1980; *Linker et al.*, 1998; *Kopp and Ip*, 2002; *Ip and Kopp*, 2002].

[34] *Ridley* [2007] demonstrated through MHD simulations that when M_A of the solar wind drops below a threshold of approximately 3, Alfvèn wings begin form in the Earth's magnetosphere as well, becoming especially prominent as M_A drops below 1. Figure 10 is a cartoon showing the behavior of the magnetosphere under Alfvèn wing conditions. The tail of the magnetosphere has vanished and is replaced by the Alfvèn wings, and the IMF field lines within the wings have bent [*Ridley*, 2007]. It should be noted that in magnetic cloud events, the solar wind can have very low density and very strong magnetic fields, leading to very low Alfvènic mach number as well as possibly formation of Alfvèn wings.

[35] Since Alfvèn wings have a conductivity which is mismatched from the polar cap conductivity, the potential can be reflected much like with mismatched impedances on a transmission line [*Kivelson and Ridley*, 2008]. The result is a limit to the cross polar cap potential. Since the Alfvèn speed of the solar wind is proportional to the magnitude of the IMF, M_A can decrease as the IMF nears the saturation regime. Thus Alfvèn wings become more prominent and could lead to the saturation of the polar cap potential during strong solar wind driving conditions. Since M_A depends on the magnitude of the IMF and not the direction, Alfvèn wings should form and lead to the saturation of the reverse

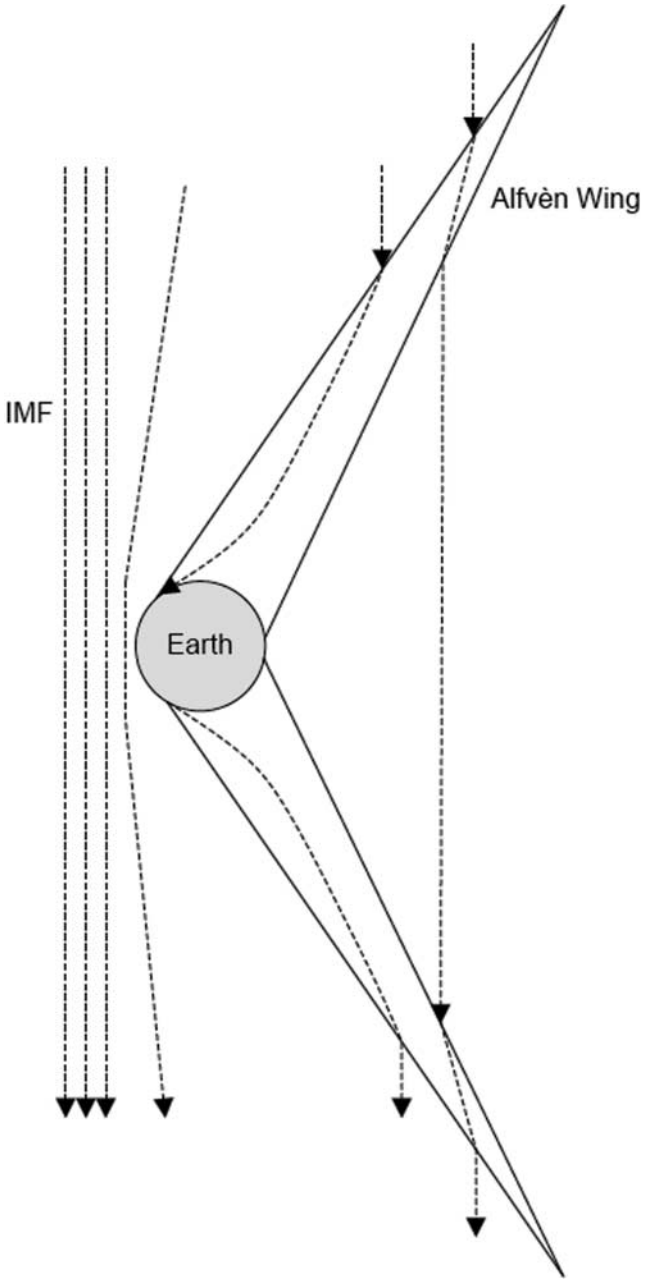

Figure 10. Alfvèn wings in the Earth's magnetosphere under southward IMF conditions. The dashed lines are magnetic field lines, and the solid lines define the boundary of the Alfvèn wings.

convection potential under northward IMF as well [*Ridley*, 2007].

[36] In order to test the dependence of Φ_{RC} on M_A, first it will be useful to see the distribution of M_A for events within the linear and saturation regimes of Figure 4. If Alfvèn wings are a fundamental cause of saturation under northward IMF, then one would expect to see significantly lower M_A in the solar wind for the saturation regime of Figure 4. Events were organized based on whether they were stable within 8–17 kV/Re for the linear regime or within 25 to 60 kV/Re for the saturated regime of Figure 4. The mean M_A was then calculated for each event.

[37] Figure 11 shows the histograms for (1) the linear regime and (2) the saturated regime. The linear regime does tend to have events with a larger M_A value than the saturated regime. This is to be expected, since as the IMF grows stronger, the IMF's M_A grows smaller. This does not mean, however, that the value of M_A plays a role in the mechanism by which Φ_{RC} saturates. There is still a large amount of overlap between the linear and saturated regimes, with both containing events with very small values of M_A as well as events with nominal values of M_A.

[38] In order to determine if the events with nominal M_A are also contributing to the overall saturation trend of Φ_{RC}, the method for generating Figure 4 was repeated, but with an additional restriction on M_A in the event selection criteria. Not only were all events required to stay within the minimum and maximum E_{RC} value of a particular driving bin, but only events where M_A was at least 5 were used. The M_A minimum of 5 was chosen for several reasons. First, it provided the best amount of Doppler measurements to ensure that any trend in Φ_{RC} with increasing E_{RC} would be apparent. It also excludes very small values of M_A, where simulations have shown Alfvèn Wings to become more apparent [*Ridley*, 2007]. Table 1 shows the E_{RC} bins used, along with the mean and standard deviation of M_A in each bin.

[39] Figure 12 shows the behavior of the reverse convection potential as E_{RC} increases. Φ_{RC} still demonstrates saturation behavior, with a peak potential of approximately 17 kV. Since the reverse convection potential still saturates at nominal M_A, it is unlikely that Alfvèn Wings are a fundamental cause of reverse convection potential saturation under northward IMF.

[40] As a final way to examine the dependence of Φ_{RC} on M_A, events with E_{RC} ranging between 18 and 60 kV/Re were binned based on solar wind M_A. The stability criteria was that the E_{RC} stay between 18 and 60 kV/Re and that M_A stay between its specified maximum and minimum value. Overlapping bins were used to ensure the best possible view of the behavior of Φ_{RC}. Figure 13 shows how the reverse convection potential varies with respect to M_A, as well as the mean E_{RC} for each M_A bin. While at first it may seem that Φ_{RC} is decreasing with increasing M_A, the mean E_{RC} in each M_A bin is also decreasing. While this study was done in the E_{RC} driving regime where saturation occurs, variations in E_{RC} still could have an impact on small variations in Φ_{RC}. It therefore appears that M_A has little impact on the value of Φ_{RC}.

5. Ion Beta Dependence

[41] Another solar wind driving parameter which is useful for understanding magnetospheric behavior is the plasma β. This is the ratio between thermal pressure and magnetic pressure in the solar wind and is given by

$$\beta = \frac{nkT_i}{B^2/2\mu_0} \tag{5}$$

where β is the solar wind plasma beta, n is the number density, k is Boltzmann's constant, T_i is the ion temperature, and B is the magnitude of the IMF. *Scurry et al.* [1994] demonstrated that a low-β solar wind tended to lead to a higher reconnection rate on the dayside magnetopause for southward IMF. This also indicates that the upstream β in the solar wind influences the β in the magnetosheath.

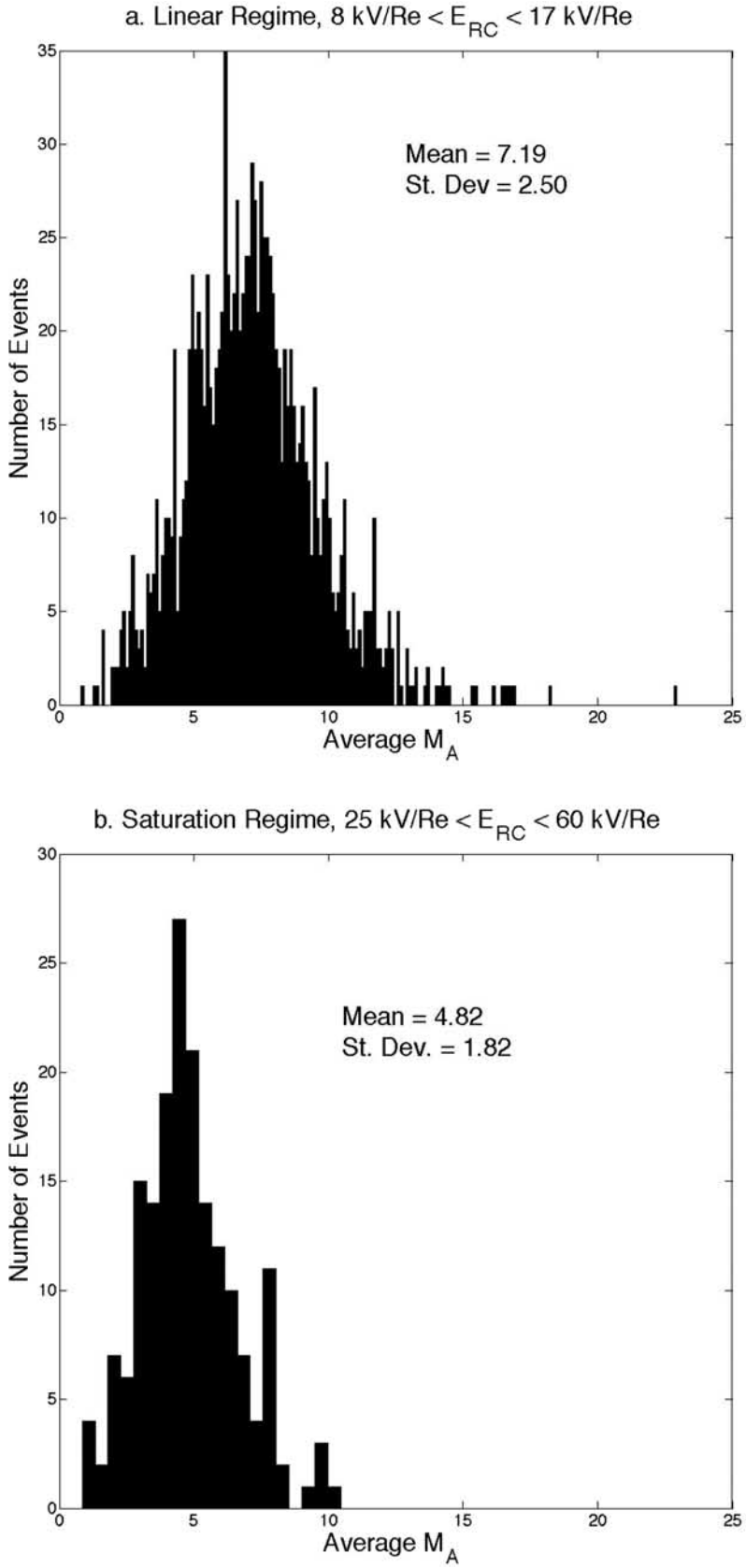

Figure 11. Histograms showing the M_A distribution for the E_{RC} ranges of (a) 8 kV/Re < E_{RC} < 17 kV/Re and (b) 25 kV/Re < E_{RC} < 60 kV/Re. The mean values of M_A in each are (a) 7.19 and (b) 4.82 with a standard deviation of (a) 2.50 and (b) 1.82.

Table 1. Bins of E_{RC} Used to Examine the Reverse Convection Potential Trend When $M_A > 3$

E_{RC} (kV/Re)	Mean M_A	Standard Deviation M_A	E_{RC} (kV/Re)	Mean M_A	Standard Deviation M_A
2–4	11.50	4.90	17–26	7.16	1.70
4–6	10.29	3.59	18–25	6.98	1.38
6–8	9.43	2.89	19–26	7.11	1.83
8–10	8.66	2.64	20–30	6.95	1.60
10–14	7.92	1.91	20–40	7.00	1.70
11–15	7.75	1.67	23–33	6.67	1.33
12–16	7.45	1.61	25–35	6.69	1.32
13–17	7.52	1.81	25–40	6.80	1.27
14–18	7.40	1.66	30–45	6.54	1.25
15–20	7.11	1.60	30–50	6.61	1.20
16–21	7.08	1.67	30–60	6.82	1.28
17–22	6.72	1.42	35–50	6.68	0.92
40–70	6.99	1.23			

Therefore understanding the effect of β on the reverse convection potential may shed light onto the effect of both reconnection and the shape of the magnetosphere. At low β, there is a high magnetic pressure, which leads to stiff frozen-in magnetic field lines and a faster reconnection rate. At high β, there is high thermal pressure, which can contribute to increased compression of the magnetosphere.

[42] The first thing examined was the distribution of solar wind plasma β for both the linear and saturated driving regimes in Figure 4. Once again, events were organized based on whether they were stable within 8–17 kV/Re for the linear regime or within 25 to 60 kV/Re for the saturated regime of Figure 4. The mean value of β was then calculated for each event. Figure 14 shows the distribution of solar wind plasma β for the linear and saturated regimes. The distributions seem to be comparable, with slightly lower β in the saturated regime. This is to be expected, since plasma β is inversely proportional to the IMF magnitude squared.

[43] To investigate the effect of plasma β on Φ_{RC} during strong driving, events with E_{RC} between 18 and 60 kV/Re were binned based on solar wind plasma β. The stability criteria was that the E_{RC} stay between 18 and 60 kV/Re and that β stay between its specified maximum and minimum value. Overlapping bins were used to ensure the best possible view of the behavior of Φ_{RC}. Figure 15 shows how the reverse convection potential varies with respect to β, as well as the mean E_{RC} for each β bin. While the mean E_{RC} in each bin stays constant, as β increases, there is an apparent increasing trend for Φ_{RC}. At extremely low β, there also seems to be larger Φ_{RC} values, but with the significantly stronger E_{RC} for the $0 < \beta < 0.05$ bin, no definite conclusions can be made.

[44] It should also be noted that for $\beta > 1.0$, the potential pattern gets too distorted to discern a reverse convection potential. This is most likely caused by the magnetosphere being highly compressed during high-β events, as high-β often corresponds with a high solar wind density and therefore larger dynamic pressure. The increased compression of the magnetosphere could also lead to the apparent increase in reverse convection potential as β increases.

6. Summary and Discussion

[45] The results presented in this study elucidate on the behavior of the four cell convection pattern under northward IMF. It is apparent that while Φ_{RC} under northward IMF is much smaller than Φ_{PC} under southward IMF, their respective electric fields are comparable. It is thus perhaps useful to discuss transpolar potential saturation in terms of polar cap electric field in addition to potential. It also indicates that there may be a connection between the saturation

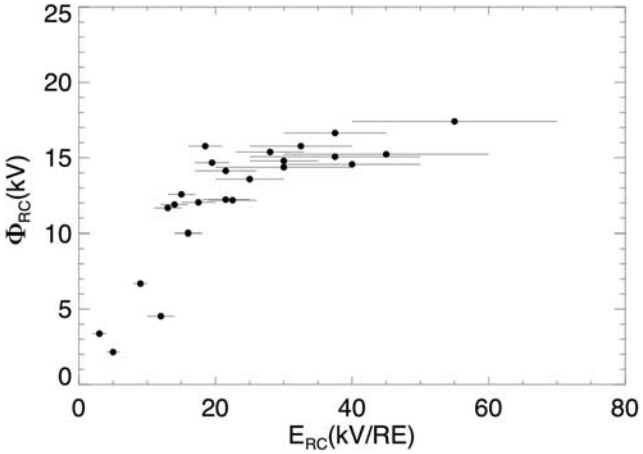

Figure 12. Reverse convection potential, Φ_{RC}, as a function of E_{RC}, for $M_A > 5$. The marks represent the center of the bins, and the horizontal lines represent the width of each bin in kV/Re.

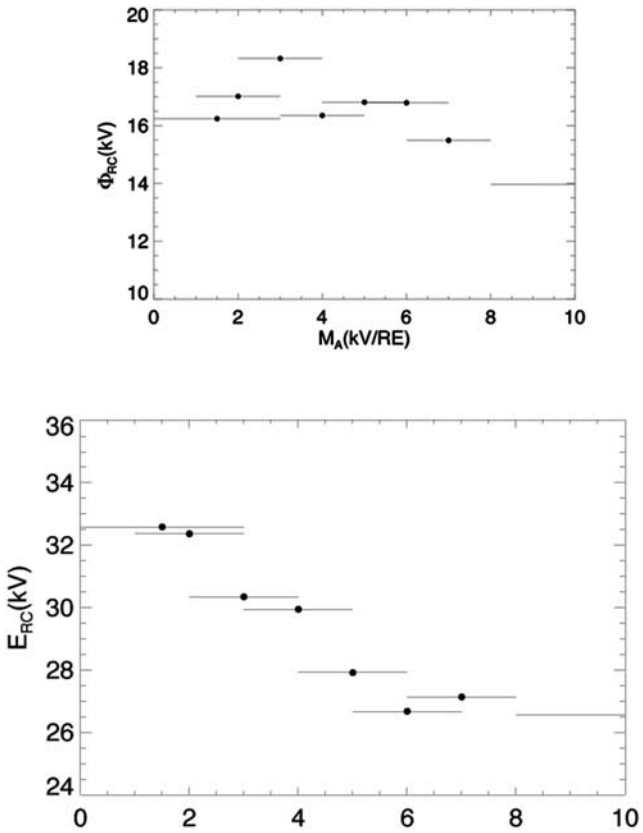

Figure 13. Statistics on the reverse convection potential for E_{RC} driving in the saturation regime and varying M_A. The top is the reverse convection potential and the bottom is the mean E_{RC} for each M_A bin.

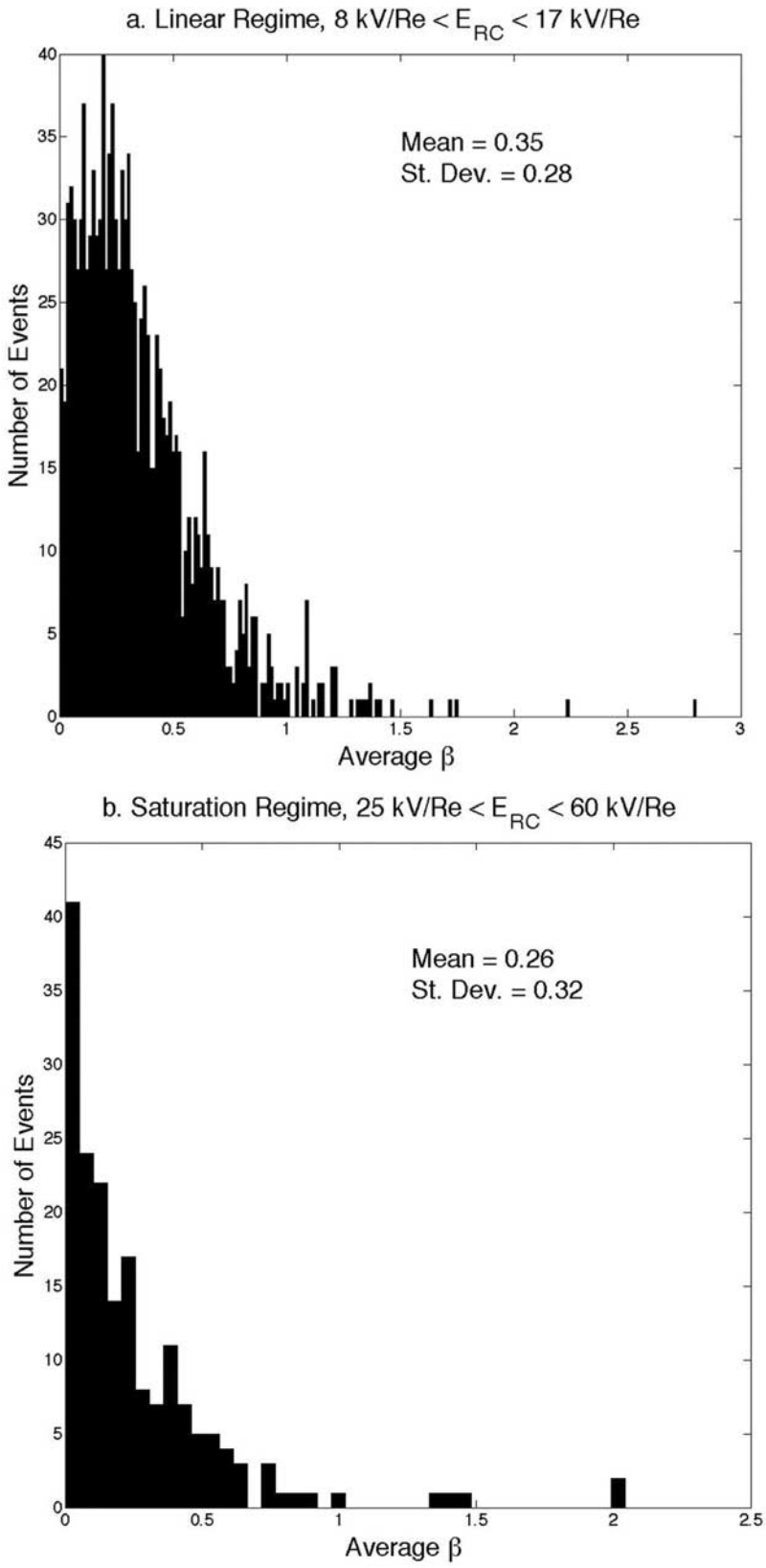

Figure 14. Histograms showing the β distribution for the E_{RC} ranges of (a) 8 kV/Re < E_{RC} < 17 kV/Re and (b) 25 kV/Re < E_{RC} < 60 kV/Re. The mean values of β in each are (a) 0.35 and (b) 0.26 with a standard deviation of (a) 0.28 and (b) 0.32.

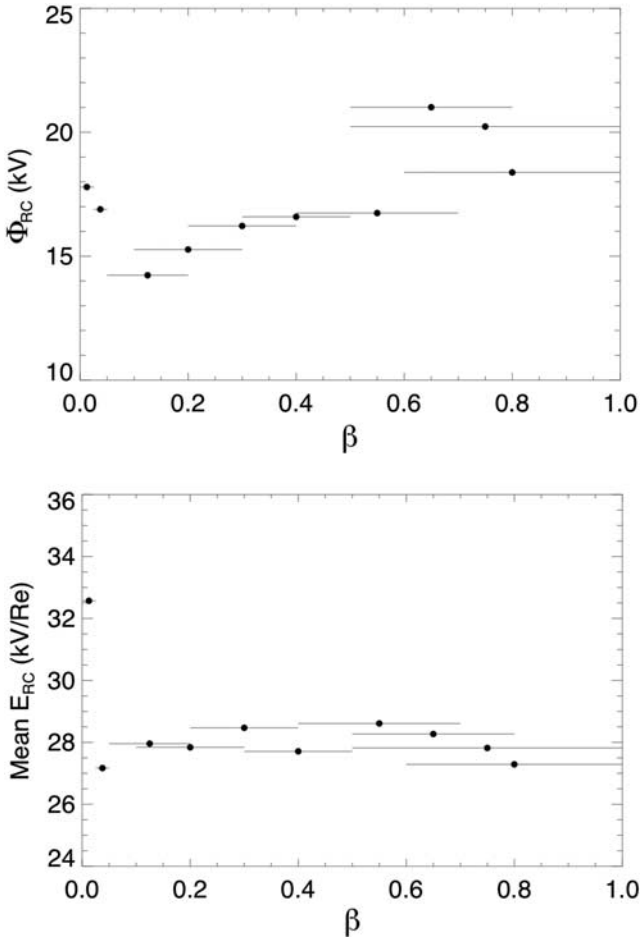

Figure 15. Statistics on the reverse convection potential for E_{RC} driving in the saturation regime and varying beta. The top is the reverse convection potential and the bottom is the mean E_{RC} for each β bin.

phenomena under northward IMF and southward IMF, as they seem to have a similar polar cap electric field limit.

[46] The seasonal variation of the four cell convection pattern under northward IMF was also investigated. While the viscous potential cells in the pattern become much stronger under low-conductivity winter months, the opposite seems to occur for the NBZ cells. This indicates that the NBZ currents may close with the region 1 field aligned currents, and that as the convection in the magnetosphere caused by viscous interactions becomes stronger, so does this coupling. A detailed study of the relationship between the NBZ currents and the region 1 and 2 field aligned currents will be necessary to determine the precise nature of their coupling under strong northward IMF.

[47] In recent years, several possible explanations for the saturation of Φ_{PC} under southward IMF have been put forth. One such explanation is that the strength of region 1 field aligned currents increase until their $\mathbf{J} \times \mathbf{B}$ force replaces that of the Chapman-Ferraro current system as the main counter to solar wind ram pressure [*Siscoe et al.*, 2002a]. Similar models also rely on strong region 1 field aligned currents which erode the magnetopause, limiting reconnection [*Siscoe et al.*, 2004]. Since NBZ currents are generated by lobe reconnection on the poleward side of the cusp, these two mechanisms are unlikely candidates to be the source for the saturation of the reverse convection potential.

[48] Another hypothesis is that saturation occurs at low solar wind Alfvènic Mach number. In this model, Alfvèn wings form in the magnetosphere, and their conductivity reduces the electric potential across the polar cap [*Ridley*, 2007; *Kivelson and Ridley*, 2008]. Since the solar wind Alfvèn speed depends on the magnitude of the IMF and not the direction, Alfvèn wings should form under northward IMF and have the same effect on Φ_{RC}.

[49] It was demonstrated through Figures 11, 12 and 13 that saturation of the reverse convection potential still occurs at nominal M_A. While this does not discount the possibility of Alfvèn wings forming in the magnetosphere under northward IMF, it does indicate that they are not the fundamental mechanism by which the reverse convection potential saturates.

[50] With regards to solar wind plasma β, its distribution is comparable in both the linear and saturated regimes of Φ_{RC}. However, as β increases, the average Φ_{RC} over the saturated regime also seems to increase. This points to the fact that as the magnetosphere becomes more compressed, the reverse convection potential either becomes less saturated, or perhaps even more linear with respect to E_{RC}. At low β, there appears to also be an increase in Φ_{RC}, which is consistent with research showing that as the solar wind β decreases, so does β in the magnetosheath, which increases the reconnection rate. Individual case studies will need to be examined; however, in order to determine just how much of an effect this has.

[51] It is evident that at present there is much to learn about the behavior of the magnetosphere and ionosphere under northward IMF. It appears that coupling can be just as strong as in southward IMF, but that the coupling is much more localized. Also, many of the hypotheses presented for saturation under southward IMF do not apply to the reverse convection potential. Future studies should be implemented to compare these two orientations of the IMF, as well as to determine the cause of electric field saturation in the polar cap.

[52] **Acknowledgments.** This research is supported by the National Science Foundation through grants ATM-0728538 and ATM-0849031 and by NASA through grant NNG05GE25G to the Virginia Polytechnic Institute and State University. Operation of the Northern Hemisphere SuperDARN radars is supported by the national funding agencies of Canada, France, Japan, the United Kingdom, and the United States.

[53] Zuyin Pu thanks the reviewers for their assistance in evaluating this paper.

References

Axford, W., and C. Hines (1961), A unifying theory of high-latitude geophysical phenomena and geomagnetic storms, *Can. J. Phys.*, *39*, 1433.

Chisham, G., et al. (2007), A decade of the super dual auroral radar network (SuperDARN): Scientific achievements, new techniques and future directions, *Surv. Geophys.*, *28*(1), 33.

Crooker, N. U. (1992), Reverse convection, *J. Geophys. Res.*, *97*, 19,363.

Dorelli, J., A. Bhattacharjee, and J. Raeder (2007), Separator reconnection at Earth's dayside magnetopause under northward interplanetary magnetic field conditions, *J. Geophys. Res.*, *112*, A02202, doi:10.1029/2006JA011877.

Drayton, R. A., A. V. Koustov, M. R. Hairston, and J.-P. Villain (2005), Comparison of DMSP cross-track ion drifts and SuperDARN line-of-sight velocities, *Ann. Geophys.*, *23*, 2479.

Dungey, J. (1963), The structure of the exosphere or adventures in velocity space, in *Geophysics, The Earth's Environment*, edited by C. DeWitt, J. Hieblot, and A. Lebeau, 505 pp., Gordon and Breach, New York.

Dungey, J. W. (1961), Interplanetary magnetic field and the auroral zones, *Phys. Rev. Lett.*, *6*, 47.

Fujii, R., T. Ijima, T. Potemra, and M. Sugiura (1981), Seasonal dependence of large-scale Birkeland currents, *Geophys. Res. Lett.*, *8*, 1103.

Hairston, M. R., K. A. Drake, and R. Skoug (2005), Saturation of the ionospheric polar cap potential during the October-November 2003 superstorms, *J. Geophys. Res.*, *110*, A09S26, doi:10.1029/2004JA010864.

Iijima, T., T. A. Potemra, L. J. Zanetti, and P. F. Bythrow (1984), Large-scale Birkeland currents in the dayside polar region during strongly northward IMF: A new Birkeland current system, *J. Geophys. Res.*, *89*, 7441.

Ip, W. H., and A. Kopp (2002), Resistive MHD simulations of Ganymede's magnetosphere: 2. Birkeland currents and particle energetics, *J. Geophys. Res.*, *107*(A12), 1491, doi:10.1029/2001JA005072.

Jackson, J. D. (1975), *Classical Electrodynamics*, John Wiley, New York.

Kan, J. R., and L. C. Lee (1979), Energy coupling function and solar wind magnetosphere dynamo, *Geophys. Res. Lett.*, *6*, 577.

King, J. H., and N. E. Papitashvili (2005), Solar wind spatial scales in and comparisons of hourly wind and ACE plasma and magnetic field data, *J. Geophys. Res.*, *110*, A02104, doi:10.1029/2004JA010649.

Kivelson, M. G., and A. J. Ridley (2008), Saturation of the polar cap potential: Inference from Alfvèn wing arguments, *J. Geophys. Res.*, *113*, A05214, doi:10.1029/2007JA012302.

Kopp, A., and W. H. Ip (2002), Resistive MHD simulations of Ganymede's magnetosphere: 1. Time variabilities of the magnetic field topology, *J. Geophys. Res.*, *107*(A12), 1490, doi:10.1029/2001JA005071.

Linker, J. A., K. K. Khurana, M. G. Kivelson, and R. J. Walker (1998), MHD simulation of Io's interaction with the plasma torus, *J. Geophys. Res.*, *103*, 19,867.

Neubauer, F. (1980), Nonlinear standing Alfvèn wave current system at Io: Theory, *J. Geophys. Res.*, *85*, 1171.

Papitashvili, V. O., O. A. Troshichev, D. S. Faermark, and A. N. Zaitzev (1981), Linear dependence of the intensity of geomagnetic variations in the polar region on the magnitudes of the southern and northern components of the interplanetary magnetic field, *Geomagn. Aeron.*, Engl. Transl., *21*, 565.

Pearson, F. (1990), *Map Projections: Theory and Applications*, CRC Press, Boca Raton.

Rastätter, P., M. Hesse, M. Kuznetsova, J. Sigwarth, J. Raeder, and T. Gombosi (2005), Polar cap size during 14–16 July 2000 (Bastille day) solar coronal mass ejection event: MHD modeling and satellite imager observations, *J. Geophys. Res.*, *110*, A07212, doi:10.1029/2004JA010672.

Reiff, P., R. Spiro, and T. Hill (1981), Dependence of polar cap potential on interplanetary parameters, *J. Geophys. Res.*, *86*, 639.

Ridley, A. (2007), Alfvèn wings at the Earth's magnetosphere under strong interplanetary magnetic field, *Ann. Geophys.*, *23*, 533.

Ruohoniemi, J., and S. K. Baker (1998), Large-scale imaging of high-latitude convection with Super Dual Auroral Radar Network HF radar observations, *J. Geophys. Res.*, *103*, 20,797.

Scurry, L., C. T. Russel, and J. T. Gosling (1994), Geomagnetic activity and the beta dependence of the dayside reconnection rate, *J. Geophys. Res.*, *99*, 14,811.

Shepherd, S., R. Greenwald, and J. Ruohoniemi (2002), Cross polar cap potentials measured with Super Dual Auroral Radar Network during quasi-steady solar wind and interplanetary magnetic field conditions, *J. Geophys. Res.*, *107*(A7), 1094, doi:10.1029/2001JA000152.

Siscoe, G., J. Raeder, and A. Ridley (2004), Transpolar potential saturation models compared, *J. Geophys. Res.*, *109*, A09203, doi:10.1029/2003JA010318.

Siscoe, G. L., N. U. Crooker, and K. D. Siebert (2002a), Transpolar potential saturation: Roles of region 1 current system and solar wind ram pressure, *J. Geophys. Res.*, *107*(A10), 1321, doi:10.1029/2001JA009176.

Siscoe, G. L., G. M. Erickson, B. U. O. Sonnerup, N. C. Maynard, J. A. Schoendorf, K. D. Siebert, D. R. Weimer, W. W. White, and G. R. Wilson (2002b), Hill model of transpolar potential saturation: Comparisons with MHD simulations, *J. Geophys. Res.*, *107*(A6), 1075, doi:10.1029/2001JA000109.

Sonnerup, B. U. O. (1974), Magnetopause reconnection rate, *J. Geophys. Res.*, *79*, 1546.

Sundberg, K. A. T., J. A. Cumnock, and L. G. Blomberg (2009), Reverse convection potential: A statistical study of the general properties of lobe reconnection and saturation effects during northward IMF, *J. Geophys. Res.*, *114*, A06205, doi:10.1029/2009JA014069.

Watanabe, M., K. Kabin, G. J. Sofko, R. Rankin, T. I. Gombosi, A. J. Ridley, and C. R. Clauer (2005), Internal reconnection for northward interplanetary magnetic field, *J. Geophys. Res.*, *110*, A06210, doi:10.1029/2004JA010832.

Weimer, D. (1995), Models of high-latitude electric potentials derived with a least error fit of spherical harmonic coefficients, *J. Geophys. Res.*, *100*, 19,595.

Wilder, F. D., C. R. Clauer, and J. B. H. Baker (2008), Reverse convection potential saturation during northward IMF, *Geophys. Res. Lett.*, *35*, L12103, doi:10.1029/2008GL034040.

Xu, L., A. V. Koustov, J. S. Xu, R. A. Drayton, and L. Huo (2007), A 2-D comparison of ionospheric convection derived from SuperDARN and DMSP measurements, *Adv. Space Res.*, *47*, 1259.

J. B. H. Baker, C. R. Clauer, and F. D. Wilder, Bradley Department of Electrical and Computer Engineering, Virginia Tech, 203 Whittemore Hall, Blacksburg, VA 24060, USA. (fwilder@vt.edu)